



1 **Multiwavelength fluorescence lidar observations of fresh smoke plumes**

2 Igor Veselovskii<sup>1</sup>, Nikita Kasianik<sup>1</sup>, Mikhail Korenskii<sup>1</sup>, Qiaoyun Hu<sup>2</sup>, Philippe Goloub<sup>2</sup>, Thierry  
3 Podvin<sup>2</sup>, Dong Liu<sup>3</sup>

4 <sup>1</sup>*Prokhorov General Physics Institute of the Russian Academy of Sciences, Moscow, Russia.*

5 <sup>2</sup>*Univ. Lille, CNRS, UMR 8518 - LOA - Laboratoire d'Optique Atmosphérique, F-59650 Lille,*  
6 *France*

7 <sup>3</sup>*State Key Laboratory of Modern Optical Instrumentation, College of Optical Science and*  
8 *Engineering: International Research Center for Advanced Photonics, Zhejiang University,*  
9 *Hangzhou 310027, China*

10

11 Correspondence: Philippe Goloub (philippe.goloub@univ-lille.fr)

12

13 **Abstract**

14 A five-channel fluorescence lidar was developed for the study of atmospheric aerosol.  
15 The fluorescence spectrum induced by 355 nm laser emission is analyzed in five spectral  
16 intervals using interference filters. Central wavelengths and the widths of these five interference  
17 filters are respectively: 438/29, 472/32, 513/29, 560/40 and 614/54 nm. The relative calibration  
18 of these channels has been performed using a tungsten-halogen lamp with color temperature  
19 2800K. This new lidar system was operated during Summer – Autumn 2022, when strong forest  
20 fires occurred in the Moscow region and generated a series of smoke plumes analyzed in this  
21 study. Our results demonstrate that, for urban aerosol, the maximal fluorescence backscattering  
22 is observed in 472 nm channel. For the smoke the maximum is shifted toward longer  
23 wavelengths, and the fluorescence backscattering coefficients in 472 nm, 513 nm and 560 nm  
24 channels have comparable value. Thus, from the analysis of the ratios of fluorescence  
25 backscattering in available channels, we show that it is possible to identify smoke layers. The  
26 particle classification based on single channel fluorescence capacity (ratio of the fluorescence  
27 backscattering to elastic one), has limitations at high relative humidity (RH). Fluorescence  
28 capacity is indeed decreasing when water uptake of particles enhances the elastic scattering.  
29 However, the spectral variation of fluorescence backscattering does not evidence any  
30 dependence on RH and can be therefore considered for aerosol identification.

31



32           **1. Introduction**

33           The knowledge of the chemical composition of atmospheric aerosol is important for  
34 characterization of its impact on the Earth radiation balance (Boucher et al., 2013; IPCC 2022).  
35 The composition of aerosol, however, is strongly variable, and in practice, several general  
36 aerosol types, usually, are considered, based of their origin (Dubovik et al., 2002). The Mie-  
37 Raman and high spectral resolution lidars provide the opportunity to derive vertical distribution  
38 of the particle extinction and backscattering coefficients together with multispectral  
39 depolarization ratio. Based on these observations the main aerosol types can be distinguished  
40 (Burton et al., 2012, 2013; Groß et al., 2013; Mamouri et al., 2017; Papagiannopoulos et al.,  
41 2018; Nicolae et al., 2018; Hara et al., 2018; Wang et al., 2021; Mylonaki et al., 2021). However,  
42 due to the variability of aerosol parameters, the particle intensive properties (properties that are  
43 independent on concentration), such as lidar ratios, depolarization ratios and Angstrom  
44 exponents can vary in a wide range, even for aerosols from the same origin, which complicates  
45 their identification.

46           The fluorescence measurements provide new independent information about aerosol  
47 composition, which can be used for classification. (Veselovskii et al., 2022b). Being induced by  
48 355 nm laser radiation the atmospheric fluorescence emission spreads in a wide spectral range  
49 from approximately 380 nm to beyond 700 nm. The multianode photomultipliers combined with  
50 spectrometer, in principle, allow profiling the full fluorescence spectrum (Sugimoto et al., 2012;  
51 Saito et al., 2022; Reichardt et al., 2022). In a more simple approach a single fluorescence  
52 channel has been integrated into existing multiwavelength Mie-Raman lidar (Veselovskii et al.,  
53 2020), and a fraction of the fluorescence spectrum is selected by a wideband interference filter.  
54 High transmittance of modern interference filters (above 95%), allows efficient detection of  
55 fluorescence emission, and when combined with simultaneous depolarization measurements the  
56 main aerosol types, such as dust, smoke, pollen and urban can be identified (Veselovskii et al.,  
57 2022b). This classification scheme relies on the fluorescence capacity  $G_\lambda$ , which is the ratio of  
58 fluorescence backscattering to elastic backscattering at laser wavelength. The fluorescence  
59 capacity, however, depends on the relative humidity (RH), because enhanced elastic  
60 backscattering leads to decrease of  $G_\lambda$  (Veselovskii et al., 2021). Thus, at high RH, we cannot  
61 attribute unambiguously the decrease of  $G_\lambda$  to some water uptake to some changes in the aerosol  
62 composition.



63           The water uptake increases the elastic backscattering but normally does not alter the  
64 chemical components thus, total amount of fluorescent molecules within a particle does not  
65 change. The illumination intensity distribution within a particle, as well as the emission angular  
66 distribution can be altered by the change of particle size and refractive index during the  
67 hygroscopic growth. However, this effect occurs for relatively big microspheres with size  
68 parameter exceeding approximately 10 (Veselovskii et al., 2002). Thus, fluorescence of the fine  
69 mode particles should be less influenced by the hygroscopic growth. Our existing lidar data-base  
70 in well mixed boundary layer situations demonstrate that, at least, for urban and smoke particles,  
71 the fluorescence backscattering coefficient did not change during water uptake. Thus, we have  
72 good reason to expect, that fluorescence spectrum is not modified by the aerosol hygroscopic  
73 growth, and several fluorescence channels should provide more reliable information upon  
74 aerosol type.

75           Smoke is one of the most abundant aerosol types and it was intensively studied with Mie-  
76 Raman lidars for decades (Adam et al., 2021 and references therein). Smoke is characterized also  
77 by high fluorescence capacity, thus fluorescence lidar measurements proved to be very efficient  
78 for smoke identification and analysis (Hu et al., 2022, Veselovskii et al., 2022a,b). However, as  
79 mentioned, at high RH classification of smoke, based on a single channel fluorescence may fail.  
80 The solution could be the detection of fluorescence at several wavelengths. In July 2022 a new  
81 lidar system equipped with five fluorescence channels, was assembled in Prokhorov General  
82 Physics Institute, Troitsk, Moscow. The lidar was in operation during Summer and Autumn  
83 2022, when strong forest fires occurred in the Moscow region. In this paper we analyze the  
84 spectral dependence of the fluorescence backscattering inside and outside the smoke plumes. The  
85 results demonstrate that the hygroscopic growth does not affect the spectral dependence of  
86 fluorescence backscattering.

87

## 88           **2. Experimental setup**

89           The fluorescence lidar is based on a tripled Nd:YAG laser with pulse energy of 80 mJ at  
90 355 nm and repetition rate of 20 Hz. Backscattered light is collected by a 40 cm aperture  
91 Newtonian telescope and the lidar signals are digitized with Licel transient recorders with 7.5 m  
92 range resolution, allowing simultaneous detection in the analog and photon counting modes. The  
93 optical scheme of the receiving module is presented in Fig.1. The system is designed to detect



94 elastic backscattering at 355 nm, nitrogen Raman backscattering at 387 nm and fluorescence  
95 backscattering in five spectral intervals. These intervals are separated with dichroic beamsplitters  
96 and isolated by the interference filters manufactured by Alluxa. The central wavelengths and the  
97 widths of transmission bands (FWHM) of these fluorescence channels are respectively: 438/29,  
98 472/32, 513/29, 560/40 and 614/54 nm. The transmission of the filters exceeds 97%, while  
99 suppression of optical signal out of band is above OD6. To improve the suppression of elastic  
100 backscattering we installed two filters in tandem in every channel.

101 Laser radiation at 532 nm can induce additional aerosol fluorescence which will  
102 contaminate long-wave channels. To remove potential contamination, the emission at 532 nm  
103 and 1064 nm are separated with dichroic mirrors and redirected to an optical dump. Therefore,  
104 the laser beam sent into the atmosphere has only one wavelength - 355 nm. As follows from  
105 Fig.1, the 532 nm radiation is out of the transmission band of the filters, which prevents the  
106 leaking of residual 532 nm component to the fluorescence channels. We should mention, that the  
107 vibrational overtone of N<sub>2</sub> Raman scattering at 424.4 nm is within the transmission band of 438  
108 nm channel. In accordance with results of Knippers et al. (1985), Raman intensity of this  
109 overtone is about three orders lower than intensity of N<sub>2</sub> fundamental vibration (for 488 nm laser  
110 wavelength). Based on our measurements, contribution of N<sub>2</sub> overtone to fluorescence signal  
111 from urban aerosol (with backscattering coefficient of 1.0 Mm<sup>-1</sup>sr<sup>-1</sup> at 355 nm and  $G_{438}=0.3 \times 10^{-4}$   
112 <sup>4</sup>) is estimated to be below 5% at 1000 m height. In all the channels the PMTs R9880U-01 were  
113 used, except in the 614 nm channel, where R9880-20 PMT was installed, due to its higher  
114 sensitivity in the red spectral region. The strong sunlight background at daytime restricts the  
115 fluorescence observations to only nighttime.

116 The aerosol extinction coefficients at 355 nm ( $\alpha_{355}$ ) were calculated from Raman  
117 observations as described in Ansmann et al., (1992). For calculation of backscattering coefficient  
118  $\beta_{355}$  in the presence of clouds, this method was modified (Veselovskii et al, 2022b). Additional  
119 information about atmospheric properties was available from radiosonde measurements at  
120 Dolgoprudnyi station, located about 50 km away from the observation site. It should be  
121 mentioned that the current lidar configuration does not allow measurement of the depolarization  
122 ratio.

123 The fluorescence backscattering coefficient  $\beta_{F\lambda}$  is calculated from the ratio of  
124 fluorescence signal to 387 nm nitrogen Raman signal, as described in Veselovskii et al. (2020).



125 One reminds that  $\beta_{F\lambda}$  is the integral of fluorescence backscattering over the filter transmission  
126 band  $D_\lambda$ . For calculation of  $\beta_{F\lambda}$  one needs to know the differential cross section of nitrogen  
127 Raman scattering,  $\sigma_R$ , and the relative sensitivity of the nitrogen and fluorescence detection  
128 channels. The value  $\sigma_R=2.744*10^{-30}$  cm<sup>2</sup>sr<sup>-1</sup> at 355 nm was taken from Venable et al. (2011).  
129 Sensitivity of R9880U-01 photocathode in the 387 nm - 438 nm range varies for less than 10%,  
130 so we neglect this variation and calculate relative sensitivity of the PMTs as described in  
131 Veselovskii et al. (2020). The relative sensitivity of the rest of the fluorescence channels in  
132 respect to the 438 nm one, was calculated from laboratory measurements using a tungsten-  
133 halogen lamp Thorlabs QTH10/M with color temperature 2800K as a source, assuming this  
134 source follows the Planck blackbody emission. This procedure was performed once a week and  
135 variations of the calibration coefficients during August-September 2022 period were below 15%.

136 To compare  $\beta_{F\lambda}$  at different fluorescence channels we compute the mean backscattering  
137 coefficients per elementary spectral interval,  $B_\lambda = \frac{\beta_{F\lambda}}{D_\lambda}$ , denoted as “fluorescence spectral  
138 backscattering coefficient”. The fluorescence capacity  $G_\lambda$ , which is the ratio of the fluorescence  
139 backscattering to the elastic one, in principle, can be calculated for any laser wavelength. In our  
140 previous studies we calculated  $G_\lambda$  with respect to  $\beta_{532}$ , however, in this work, it was calculated  
141 with respect to 355 nm  $G_\lambda = \frac{\beta_{F\lambda}}{\beta_{355}}$ , since 532 nm wavelength was not available. All  $\beta_{F\lambda}$ ,  $G_\lambda$  and  
142  $B_\lambda$  profiles presented in this work were smoothed with the Savitzky – Golay method, using a  
143 second order polynomial with 21 points in the window.

144

### 145 3. Measurements and analysis

146 In August 2022 numerous smoke layers originating from the forest fires in Ryazan region  
147 (about 160 km South – East of Moscow) were detected over the lidar station. The travel time of  
148 the layers was less than two days, thus smoke can be considered as fresh. The previous  
149 fluorescence studies of smoke plumes transported over Atlantic and including 466/44 nm  
150 fluorescence measurements revealed that fluorescence capacity (calculated for  $\beta_{532}$ ), in the  
151 absence of hygroscopic growth, varied within the range  $(2.5-5.0)\times 10^{-4}$  (Veselovskii et al., 2021,  
152 2022a,b; Hu et al., 2022). The Backscattering Angstrom Exponent (BAE) of smoke for 355/532



153 nm wavelengths, is about 2.0, and fluorescence capacity  $G_{472}$  in 472/32 nm channel (calculated  
154 for  $\beta_{355}$ ) is expected to be in the range  $(0.8-1.6)\times 10^{-4}$ . For urban aerosol corresponding  $G_{472}$   
155 should be  $(0.03-0.3)\times 10^{-4}$ . Here and below the fluorescence capacity will be provided for 472  
156 nm, because in most of the cases fluorescence in this channel was maximal.

157

### 158 **3.1. Fluorescence measurements during smoke episode**

#### 159 ***27-28 August 2022***

160 Two-day backward trajectories from the NOAA HYSPLIT model for the air mass reaching  
161 Moscow on 28 August at 00:00 UTC are shown in Fig.2. Air masses observed at 1500 m, passed  
162 over the fire region, close to the ground, and should thus contain products of biomass burning.  
163 The relative humidity measured by the radiosonde, at 00:00 UTC, was about 35% at 1000 m and  
164 increased with height up to 70% at 3000 m. Temporal evolution of the aerosol backscattering  
165 coefficient,  $\beta_{355}$ , fluorescence backscattering,  $\beta_{F438}$ , and fluorescence capacity,  $G_{472}$ , are shown in  
166 Fig.3. Aerosols are localized mainly below 3000 m, while above 4000 m cloud layers can be  
167 seen. In the boundary layer the fluorescence backscattering inside the boundary layer is the  
168 strongest before 20:30 UTC. The fluorescence capacity exceeds  $2.5\times 10^{-4}$ , which is the highest  
169 observed  $G_{472}$ . After 20:30  $G_{472}$  decreases but remains above  $1.0\times 10^{-4}$ , which, in principle, can  
170 be due to mixing of smoke with urban aerosol.

171 Vertical profiles of the fluorescence spectral backscattering coefficients  $B_{\lambda}$  are shown in  
172 Fig.4 for the period corresponding to maximum fluorescence capacity (19:00-20:00 UTC).  
173 Profiles of  $B_{472}$ ,  $B_{513}$ ,  $B_{560}$  are similar, indicating that fluorescence does not demonstrate  
174 significant spectral variations in 472-560 nm spectral range. The fluorescence capacity  $G_{472}$  is  
175 above  $2.0\times 10^{-4}$ , in 1.0 km – 2.5 km height range, where  $\beta_{355}$  and  $B_{\lambda}$  are maximum. The ratios  
176  $B_{472}/B_{438}$ ,  $B_{472}/B_{513}$ ,  $B_{472}/B_{560}$ ,  $B_{472}/B_{614}$  do not demonstrate height dependence in 1000-2500 m  
177 range, thus, the fluorescence spectrum in this interval is not changed. Fig.5 shows spectra of  
178 fluorescence for two distinct temporal intervals. In the interval corresponding to high  
179 fluorescence capacity (19:00-20:00 UTC), the maximum fluorescence backscattering is observed  
180 in 513 nm channel, which agrees with spectrum of smoke fluorescence provided by Reichard et  
181 al. (2022). In the second interval (23:00-01:00 UTC), when fluorescence capacity is lower, the  
182 fluorescence is maximal at 472 nm and at longer wavelengths it decreases fast. The lidar ratios  
183 ( $S_{355}$ ) for both time intervals are shown in the same figure. For the first interval (with maximum



184  $G_{472}$   $S_{355}$  is about 60 sr, while for the second interval  $S_{355}$  decreases to about 40 sr. Lidar ratio 60  
185 sr is in agreement with  $S_{355}$  reported for fresh smoke (Adam et al., 2021), while values about 40  
186 sr are usually observed for urban particles at low RH. The highest spectral fluorescence capacity  
187 of smoke (capacity per elementary spectral interval), reported by Reichard et al. (2022) for 455–  
188 535 nm range is about  $8 \times 10^{-6} \text{ nm}^{-1}$ . This is very comparable with our value ( $11 \times 10^{-6} \text{ nm}^{-1}$ )  
189 calculated from data plotted in Fig.4 and 5 at 472 nm in 19:00-20:00 UTC time interval.

190 The variation of the fluorescence spectra with height is revealed by the ratio of the  
191 fluorescence backscattering coefficients at different wavelengths (e.g.  $B_{472}/B_{\lambda}$ ). In particular,  
192 inside the aerosol plume in Fig.3  $B_{\lambda}$  does not change significantly in 472 – 560 nm range, so the  
193 ratios  $B_{472}/B_{513}$ ,  $B_{472}/B_{560}$  are close to 1.0. Temporal evolution of these ratios is shown in the right  
194 column in Fig.3. The intervals with the maximum  $G_{472}$  are well distinguished by minimum  
195  $B_{472}/B_{513}$  and  $B_{472}/B_{560}$  ratios. At the same time, ratio  $B_{472}/B_{438}$  appears to be less sensitive to  $G_{472}$   
196 changes. Actually, this ratio even increases inside the aerosol plume. Thus, the analysis of Fig.3  
197 reveals two types of the particles. The first type having a high fluorescence capacity  
198 ( $G_{472} > 2.0 \times 10^{-4}$ ) and a lidar ratio close to 60 sr can be classified as “pure” smoke. The second  
199 type, with lower fluorescence capacity ( $G_{472} \sim 1 \times 10^{-4}$ ) and a smaller lidar ratio, can be a mixture  
200 of smoke and urban aerosol.

201 Forest fires stopped in the beginning of September, so during September – October the  
202 urban aerosols were predominant. Fig.6 shows corresponding fluorescence spectra, normalized  
203 to  $B_{472}$ . Measurements were performed during 07:00-09:00 UTC and averaged within the  
204 boundary layer between 500 m and 1000 m. For urban aerosols, fluorescence at wavelengths  
205 larger than 472 nm decreases fast. Presence of remaining smoke, however, may lead to some  
206 increase of  $B_{\lambda}$  in the 513 – 614 nm interval. For urban aerosol particles the fluorescence capacity  
207  $G_{472}$  for urban particles varied within  $(0.1-0.4) \times 10^{-4}$  and the lidar ratios within 30-50 sr interval.  
208 Thus, a mixture of smoke and urban particles can explain the variability observed in fluorescence  
209 spectrum on Fig.5.

210

### 211 **17 August 2022**

212 The spatio – temporal intervals with high fluorescence capacity were observed also for  
213 other days. On August 17-18, 2022 between 18:00 – 19:00 UTC, fluorescence capacity at 472  
214 nm, the  $G_{472}$ , within the aerosol plume increased above  $1.0 \times 10^{-4}$  (Fig.7). Simultaneously, the





215 ratio  $B_{472}/B_{560}$  decreases to less than 0.8. Outside the plume, the fluorescence capacity is (0.4-  
216  $0.7) \times 10^{-4}$  and the ratio  $B_{472}/B_{560}$  increases up to 1.5. Corresponding fluorescence spectra are  
217 shown in Fig.8. Inside the plume the fluorescence is maximal in the 560 nm channel, while  
218 outside the maximum is shifted to 472 nm. Similarly to the 27-28 August event (Fig.5), the lidar  
219 ratio  $S_{355}$  is about 60 sr inside the plume and decreases down to about 30 sr outside the plume.  
220 Thus, again, we conclude that in the interval having the highest  $G_{472}$ , smoke particles are  
221 predominant, while outside we very likely addressed a mixture of smoke and urban aerosol.

222

### 223 **3.2. Analysis of fluorescence profiles observed in the presence of hygroscopic** 224 **growth of aerosol.**

225 Our previous studies with a single channel fluorescence lidar revealed, that the  
226 hygroscopic growth of aerosol particles decreases the fluorescence capacity, but does not affect  
227 the fluorescence backscattering coefficient (Veselovskii et al, 2021). Thus, when fluorescence  
228 spectra are available, one can expect that spectral dependence of fluorescence backscattering  
229 coefficients will preserve information about particle type (will not be influenced by water  
230 uptake). Below, we provide interpretation of the measurements performed during the nights  
231 August 21-22 and 23-24 2022. In both cases, RH increased with altitude and the hygroscopic  
232 growth is one possible contributor to the observed increase of particle backscattering coefficient.  
233 Our results show, that on August 21-22 the shape of the fluorescence spectrum (the set of  $B_{\lambda}/B_{472}$   
234 ratios) did not exhibit any change with altitude, whereas, conversely, on August 23-24 the shape  
235 of the fluorescence spectrum has changed with altitude, indicating possible change of aerosol  
236 composition with height.

237 Fig.9. shows vertical profiles of the fluorescence spectral backscattering coefficients,  $B_{\lambda}$ ,  
238 together with backscattering  $\beta_{355}$  coefficient, fluorescence capacity  $G_{472}$ , and  $B_{472}/B_{438}$ ,  $B_{472}/B_{513}$ ,  
239  $B_{472}/B_{560}$  ratios on August 21 2022. Profiles of  $B_{472}/B_{614}$  ratio are noisier and not used for  
240 analysis. The profile of relative humidity measured by a radiosonde at Dolgoprudnii station,  
241 shows increase of RH with altitude from 30% to 80% within 1000-4500 interval. Inside 3000-  
242 4000 m range, the fluorescence backscattering does not demonstrate significant variations while  
243 elastic backscattering increases by two orders of magnitude (from approximately  $1 \text{ Mm}^{-1}\text{sr}^{-1}$  to  
244  $100 \text{ Mm}^{-1}\text{sr}^{-1}$ ), which should be attributed to aerosol hygroscopic growth. The fluorescence  
245 capacity,  $G_{472}$ , decreases to less than  $0.01 \times 10^{-4}$  at 4000 m, however, the ratios  $B_{472}/B_{438}$ ,





246  $B_{472}/B_{513}$ ,  $B_{472}/B_{560}$  do not change with altitude, meaning that i) the spectrum (its shape) is not  
247 affected by water uptake process and that ii) aerosol composition remains constant.

248 Temporal evolution of the particle parameters on the August 23-24 night is presented in  
249 Fig.10. The relative humidity increases with height and during 18:00-20:00 time interval a cloud  
250 was formed at ~3000 m. After 20:00 the fluorescence capacity inside 2000-3000 m height range  
251 is low (below  $0.2 \times 10^{-4}$ ), however low values of  $G_{472}$  can also be explained by particle  
252 hygroscopic growth, thus one can not yet conclude that aerosol composition has changed,  
253 because the two effects (RH + aerosol changes) can occur simultaneously. Meanwhile,  $B_{472}/B_{560}$   
254 ratio decreases above 2000 m, which can be an indication of aerosol composition change.  
255 Profiles of aerosol properties for the time interval 20:30-23:30 are shown in Fig.11. In  
256 accordance with the radiosonde measurements the relative humidity reaches 80% at 3000 m at  
257 00:00 UTC. At 1000 m height, where RH is low (~35%),  $G_{472}$  is about  $0.4 \times 10^{-4}$ , hence, urban  
258 aerosol type is predominant. Both  $B_{472}/B_{513}$  and  $B_{472}/B_{560}$  ratios decrease above 2000 m, while  
259  $B_{472}/B_{438}$  increases. As mentioned above, such behavior can be an indication that contribution of  
260 smoke rises with height.

261 Normalized fluorescence spectra for two height intervals, 1000-1500 m and 2500-3000 m  
262 are shown in Fig.11c. In the second interval, the spectrum is shifted towards longer wavelengths,  
263 which corroborates that smoke fraction in the aerosol mixture increases above 2000 m. Thus, the  
264 analysis of this episode demonstrates that multi-spectral fluorescence backscattering provides  
265 opportunity for particle identification even in the presence of hygroscopic growth.

266

### 267 **Conclusions and perspectives**

268 Observations performed with a five-channel fluorescence lidar allow estimation of  
269 atmospheric aerosol fluorescence spectrum. For urban aerosol type the maximum of fluorescence  
270 is observed at 472 nm. However, for smoke particles, the maximum is shifted toward longer  
271 wavelengths and the fluorescence backscattering coefficients in the 472 nm, 513 nm and 560 nm  
272 channels are comparable. Hence, the ratios  $B_{472}/B_{513}$  or  $B_{472}/B_{560}$ , allow identification of the  
273 smoke layers because, for smoke, these ratios are smaller than for urban particles.

274 During strong forest fires in August 2022 we regularly observed over Moscow aerosol  
275 plumes, characterized by high fluorescence capacity ( $G_{472} > 1.0 \times 10^{-4}$ ). Inside these plumes, lidar  
276 ratio  $S_{355}$  increased up to 60 sr simultaneously with a shift of the fluorescence maximum to 513



277 nm or 560 nm. Particles inside plume are very likely composed of “pure” smoke, while outside  
278 the plume, a smoke/urban mixture is probable. Classification of aerosol particles based on single  
279 channel fluorescence measurements has limitations at high RH because the fluorescence capacity  
280 is decreasing due to water uptake. However, our experimental database of fluorescence  
281 backscattering ratios does not evidence noticeable dependence with RH, which means these  
282 ratios allow us to identify smoke layers even in the presence of hygroscopic growth.

283 In our measurements, the laser emitted only 355 nm radiation, however, for aerosol  
284 detailed characterization it is important to use 532 nm and 1064 nm wavelengths as well. Such  
285 Laser Induced Fluorescence Exploratory instrument (LIFE) is currently under construction and  
286 will start operation in 2023, at LOA, ATOLL platform (France), in the frame of the OBS4CLIM  
287 project and AGORA-Lab research and development activities. More generally, it seems  
288 promising to upgrade widely-used multiwavelength Mie-Raman high performance lidars with a  
289 couple of fluorescence channels. According to our results, at least for smoke, the 472 nm and  
290 513 nm channels can be considered. The wavelengths of anti-Stokes components of nitrogen  
291 and oxygen stimulated by 532 nm radiation are 473 nm and 491 nm respectively. The oxygen  
292 component is blocked by the filter, while the nitrogen one is inside the transmission band of the  
293 472 nm channel. The power of anti-Stokes scattering increases with temperature, but even at  
294 30C<sup>0</sup> its contribution to the fluorescence signal is insignificant. Estimations show that for  
295 backscattering coefficient  $\beta_{355}=1.0 \text{ Mm}^{-1}\text{sr}^{-1}$  and  $\beta_{F513}=0.2\times 10^{-4} \text{ Mm}^{-1}\text{sr}^{-1}$  (urban aerosol), the  
296 relative contribution of the nitrogen anti-Stokes component to the fluorescence at 1000 m height  
297 is below  $4\times 10^{-4}$ .

298 The results presented in this study are preliminary. We focused mainly on the fresh  
299 smoke analysis. However, smoke particle fluorescence properties depend on its chemical  
300 composition, in particular, on its organic carbon fraction. In addition, smoke fluorescence may  
301 be influenced by the burning process and transportation conditions. Thus, fluorescence spectra  
302 appears to be a relevant information to differentiate fresh from aged smoke particles. More  
303 observation campaigns, at different locations, are needed to clarify this. In the coming Spring –  
304 Summer period analysis of fluorescence spectra of different aerosol types, in particular, the  
305 pollens, is planned. At present, the system used in this study is being modified to include  
306 depolarization capability.

307



308 **Data availability.** Lidar measurements are available upon request  
309 (philippe.goloub@univ-lille.fr).

310  
311 **Author contributions.** IV assembled the lidar and wrote the paper. NK and MK performed the  
312 measurements. QH, and PG analyzed data and helped with paper preparation. TP helped with  
313 lidar design, DL participated in paper preparation.  
314 .

315 **Competing interests.** The authors declare that they have no conflict of interests.

316

### 317 **Acknowledgement**

318 Development of the lidar system was supported by Russian Science Foundation (project  
319 21-17-00114). We acknowledge funding from the CaPPA project funded by the ANR through  
320 the PIA under contract [ANR-11-LABX-0005-01](#), the “Hauts de France” Regional Council  
321 (project CLIMIBIO) and the European Regional Development Fund (FEDER). ESA/QA4EO  
322 program is greatly acknowledged for support of observation activity at LOA as well as  
323 OBS4CLIM Equipex project funded by ANR.

324



325 **References**

- 326 Adam, M., Stachlewska, I. S., Mona, L., Papagiannopoulos, N., Bravo-Aranda, J. A., Sicard, M.,  
327 Nicolae, D. N., Belegante, L., Janicka, L., Szczepanik, D., Mylonaki, M., Papanikolaou, C.-  
328 A., Siomos, N., Voudouri, K. A., Alados-Arboledas, L., Apituley, A., Mattis, I., Chaikovsky,  
329 A., Muñoz-Porcar, C., Pietruczuk, A., Bortoli, D., Baars, H., Grigorov, I., and Peshev, Z.:  
330 Biomass burning events measured by lidars in EARLINET – Part 2: Optical properties  
331 investigation, *Atmos. Chem. Phys. Discuss.*, <https://doi.org/10.5194/acp-2021-759>, in review,  
332 2021.
- 333 Ansmann, A., Riebesell, M., Wandinger, U., Weitkamp, C., Voss, E., Lahmann, W., and  
334 Michaelis, W.: Combined Raman elastic-backscatter lidar for vertical profiling of moisture,  
335 aerosols extinction, backscatter, and lidar ratio, *Appl.Phys.B*, 55, 18-28, 1992.
- 336 Boucher, O., Randall, D., Artaxo, P., Bretherton, C., Feingold, G., Forster, P., Kerminen, V.-M.,  
337 Kondo, Y., Liao, H., Lohmann, U., Rasch, P., Satheesh, S. K., Sherwood, S., Stevens, B., and  
338 Zhang, X. Y.: Clouds and Aerosols, in: *Climate Change 2013: The Physical Science Basis*.  
339 Contribution of Working Group I to the Fifth Assessment Report of the Intergovernmental  
340 Panel on Climate Change, edited by: Stocker, T. F., Qin, D., Plattner, G.-K., Tignor, M.,  
341 Allen, S. K., Boschung, J., Nauels, A., Xia, Y., Bex, V., and Midgley, P.,M., Cambridge  
342 University Press, Cambridge, United Kingdom and New York, NY, USA, 2013
- 343 Burton, S. P., Ferrare, R. A., Hostetler, C. A., Hair, J.W., Rogers, R. R., Obland, M. D., Butler,  
344 C. F., Cook, A. L., Harper, D. B., and Froyd, K. D.: Aerosol classification using airborne  
345 High Spectral Resolution Lidar measurements – methodology and examples, *Atmos. Meas.*  
346 *Tech.*, 5, 73–98, 2012. <https://doi.org/10.5194/amt-5-73-2012>
- 347 Burton, S. P., Ferrare, R. A., Vaughan, M. A., Omar, A. H., Rogers, R. R., Hostetler, C. A., and  
348 Hair, J. W.: Aerosol classification from airborne HSRL and comparisons with the CALIPSO  
349 vertical feature mask, *Atmos. Meas. Tech.*, 6, 1397–1412, 2013. [https://doi.org/10.5194/amt-](https://doi.org/10.5194/amt-6-1397-2013)  
350 [6-1397-2013](https://doi.org/10.5194/amt-6-1397-2013)
- 351 Dubovik, O., Holben, B. N., Eck, T. F., Smirnov, A., Kaufman, Y. J., King, M. D., Tanre, D.,  
352 and Slutsker, I.: Variability of absorption and optical properties of key aerosol types observed  
353 in worldwide locations, *J. Atmos. Sci.*, 59, 590–608, 2002.



- 354 Groß, S., Esselborn, M., Weinzierl, B., Wirth, M., Fix, A., and Petzold, A.: Aerosol classification  
355 by airborne high spectral resolution lidar observations, *Atmos. Chem. Phys.*, 13, 2487–2505,  
356 2013. <https://doi.org/10.5194/acp-13-2487-2013>
- 357 Hara, Y., Nishizawa, T., Sugimoto, N., Osada, K., Yumimoto, K., Uno, I., Kudo, R., and  
358 Ishimoto, H.: Retrieval of aerosol components using multi-wavelength Mie-Raman lidar and  
359 comparison with ground aerosol sampling, *Remote Sens.*, 10, 937, 2018.  
360 <https://doi.org/10.3390/rs10060937>
- 361 Hu, Q., Goloub, P., Veselovskii, I., and Podvin, T.: The characterization of long-range  
362 transported North American biomass burning plumes: what can a multi-wavelength Mie-  
363 Raman-polarization-fluorescence lidar provide? *Atmos. Chem. Phys.* 22, 5399–5414, 2022  
364 <https://doi.org/10.5194/acp-22-5399-2022>
- 365 Knippers, W., van Helvoort, K., and Stolte, S.: Vibrational overtones of the homonuclear  
366 diatomics (N<sub>2</sub>, O<sub>2</sub>, D<sub>2</sub>) observed by the spontaneous 385 Raman effect, *Chem. Phys. Lett.*,  
367 121, 279–286, 1985. [https://doi.org/10.1016/0009-2614\(85\)87179-7](https://doi.org/10.1016/0009-2614(85)87179-7)
- 368 Mamouri, R.-E., and Ansmann, A.: Potential of polarization/Raman lidar to separate fine dust,  
369 coarse dust, maritime, and anthropogenic aerosol profiles, *Atmos. Meas. Tech.*, 10, 3403–  
370 3427, 2017. <https://doi.org/10.5194/amt-10-3403-2017>
- 371 Mylonaki, M., Giannakaki, E., Papayannis, A., Papanikolaou, C.-A., Komppula, M., Nicolae, D.,  
372 Papagiannopoulos, N., Amodeo, A., Baars, H., and Soupiona, O.: Aerosol type classification  
373 analysis using EARLINET multiwavelength and depolarization lidar observations, *Atmos.*  
374 *Chem. Phys.*, 21, 2211–2227, 2021. <https://doi.org/10.5194/acp-21-2211-2021>
- 375 Nicolae, D., Vasilescu, J., Talianu, C., Biniotoglou, I., Nicolae, V., Andrei, S., and Antonescu,  
376 B.: A neural network aerosol-typing algorithm based on lidar data, *Atmos. Chem. Phys.*, 18,  
377 14511–14537, 2018. <https://doi.org/10.5194/acp-18-14511-2018>
- 378 Papagiannopoulos, N., Mona, L., Amodeo, A., D’Amico, G., Gumà Claramunt, P., Pappalardo,  
379 G., Alados-Arboledas, L., Guerrero-Rascado, J. L., Amiridis, V., Kokkalis, P., Apituley, A.,  
380 Baars, H., Schwarz, A., Wandinger, U., Biniotoglou, I., Nicolae, D., Bortoli, D., Comerón, A.,  
381 Rodríguez-Gómez, A., Sicard, M., Papayannis, A., and Wiegner, M.: An automatic  
382 observation-based aerosol typing method for EARLINET, *Atmos. Chem. Phys.*, 18, 15879–  
383 15901, 2018. <https://doi.org/10.5194/acp-18-15879-2018>

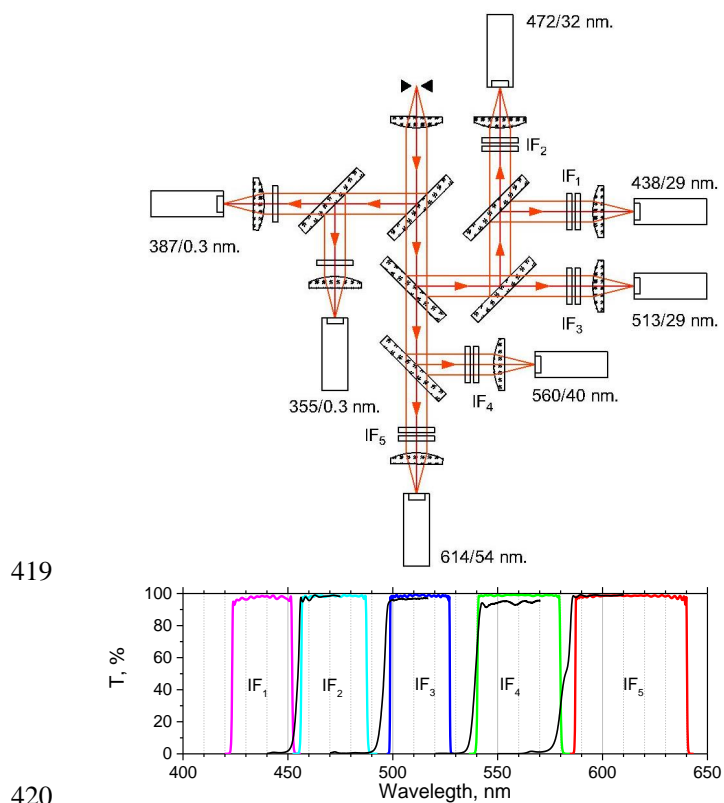


- 384 Reichardt, J., Behrendt, O., and Lauer mann, F.: Spectrometric fluorescence and Raman lidar:  
385 absolute calibration of aerosol fluorescence spectra and fluorescence correction of humidity  
386 measurements, *Atmos. Meas. Tech.*, 16, 1–13, 2023. <https://doi.org/10.5194/amt-16-1-2023>
- 387 Saito, Y., Hosokawa, T., Shiraishi, K.: Collection of excitation-emission-matrix fluorescence of  
388 aerosol-candidate-substances and its application to fluorescence lidar monitoring, *Appl. Opt.*,  
389 61, 653 – 660, 2022.
- 390 Sugimoto, N., Huang, Z., Nishizawa, T., Matsui, I., Tatarov, B.: Fluorescence from atmospheric  
391 aerosols observed with a multichannel lidar spectrometer," *Opt. Expr.* 20, 20800-20807, 2012.
- 392 Venable, D. D., Whiteman, D. N., Calhoun, M. N., Dirisu, A.O., Connell, R. M., Landulfo, E.:  
393 Lamp mapping technique for independent determination of the water vapor mixing ratio  
394 calibration factor for a Raman lidar system, *Appl. Opt.*, 50, 4622 - 4632, 2011.
- 395 Veselovskii, I., Griaznov, V., Kolgotin, A., Whiteman, D.: “Angle- and size-dependent  
396 characteristics of incoherent Raman and fluorescent scattering by microspheres 2.: Numerical  
397 simulation”, *Appl. Opt.* 41, 5783-5791, 2002
- 398 Veselovskii, I., Hu, Q., Goloub, P., Podvin, T., Korenskiy, M., Pujol, O., Dubovik, O., Lopatin,  
399 A.: Combined use of Mie-Raman and fluorescence lidar observations for improving aerosol  
400 characterization: feasibility experiment, *Atm. Meas. Tech.*, 13, 6691–6701, 2020.  
401 [doi.org/10.5194/amt-13-6691-2020](https://doi.org/10.5194/amt-13-6691-2020).
- 402 Veselovskii, I., Hu, Q., Goloub, P., Podvin, T., Choël, M., Visez, N., and Korenskiy, M.: Mie–  
403 Raman–fluorescence lidar observations of aerosols during pollen season in the north of  
404 France, *Atm. Meas. Tech.*, 14, 4773–4786, 2021. [doi.org/10.5194/amt-14-4773-2021](https://doi.org/10.5194/amt-14-4773-2021)
- 405 Veselovskii, I., Hu, Q., Ansmann, A., Goloub, P., Podvin, T., Korenskiy, N.: Fluorescence lidar  
406 observations of wildfire smoke inside cirrus: A contribution to smoke-cirrus - interaction  
407 research, *Atmos. Chem. Phys.*, 22, 5209–5221, 2022a. [https://doi.org/10.5194/acp-22-5209-](https://doi.org/10.5194/acp-22-5209-2022a)  
408 [2022a](https://doi.org/10.5194/acp-22-5209-2022a).
- 409 Veselovskii, I., Hu, Q., Goloub, P., Podvin, T., Barchunov, B., and Korenskiy, M.: Combining  
410 Mie–Raman and fluorescence observations: a step forward in aerosol classification with lidar  
411 technology, *Atmos. Meas. Tech.*, 15, 4881–4900, 2022b. [https://doi.org/10.5194/amt-15-](https://doi.org/10.5194/amt-15-4881-2022)  
412 [4881-2022](https://doi.org/10.5194/amt-15-4881-2022).
- 413 Wang, N., Shen, X., Xiao, D., Veselovskii, I., Zhao, C., Chen, F., Liu, C., Rong, Y., Ke, J., Wang,  
414 B., Qi, B., Liu, D.: Development of ZJU high-spectral-resolution lidar for aerosol and cloud:



415 feature detection and classification, Journal of Quantitative Spectroscopy & Radiative  
416 Transfer, v.261, 107513, 2021. [doi.org/10.1016/j.jqsrt.2021.107513](https://doi.org/10.1016/j.jqsrt.2021.107513)  
417  
418





419

420

421 Fig.1. Optical scheme of the receiving module of the lidar together with transmissions of  
422 interference filters IF<sub>1</sub>-IF<sub>5</sub> in the fluorescence channels. Black lines show the transmissions of the  
423 45 degree dichroic beam splitters used for separation of fluorescence spectral components.

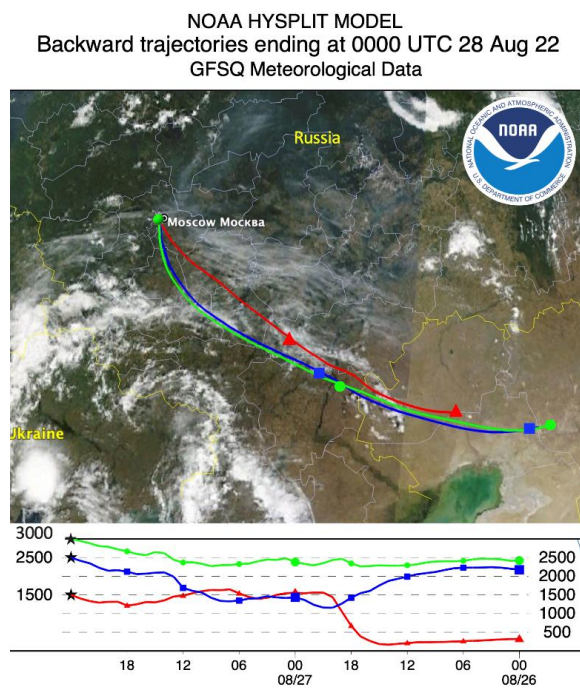
424



425

426

427



428

429

430 Fig.2. Two-day backward trajectories from the NOAA HYSPLIT model for the air mass in  
431 Moscow on 28 August at 00:00 UTC. The basemap is the Earth's true color image observed by  
432 MODIS Terra for the same period.

433



434

435

436

437

438

439

440

441

442

443

444

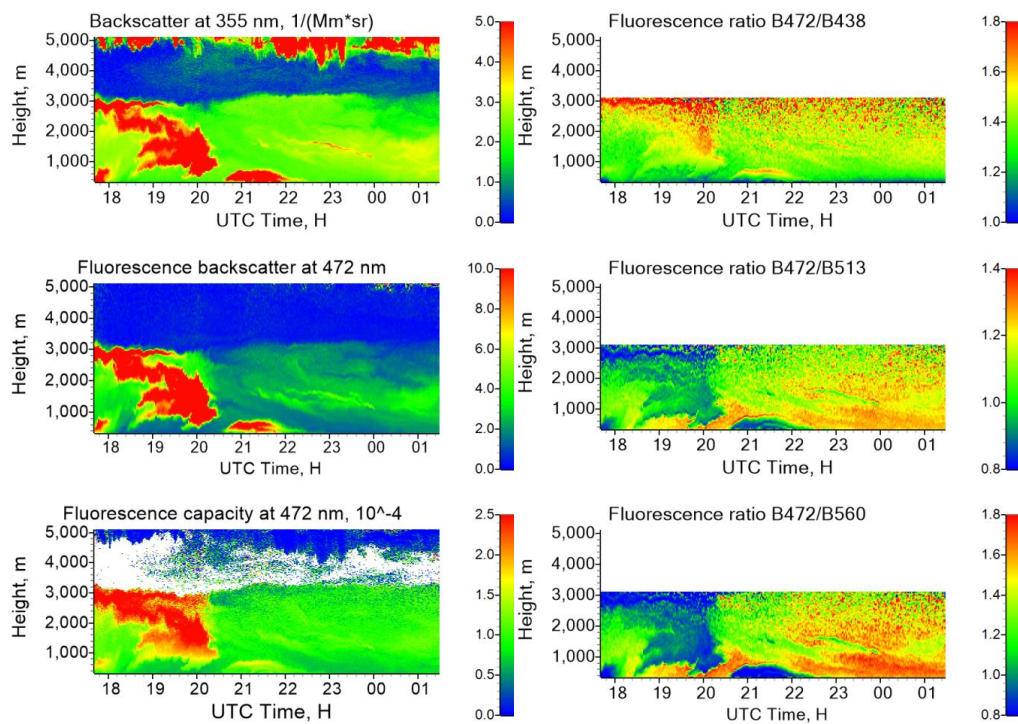
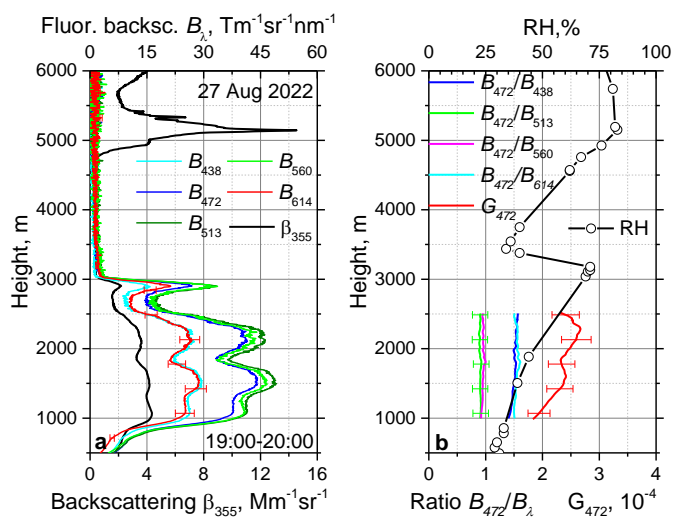
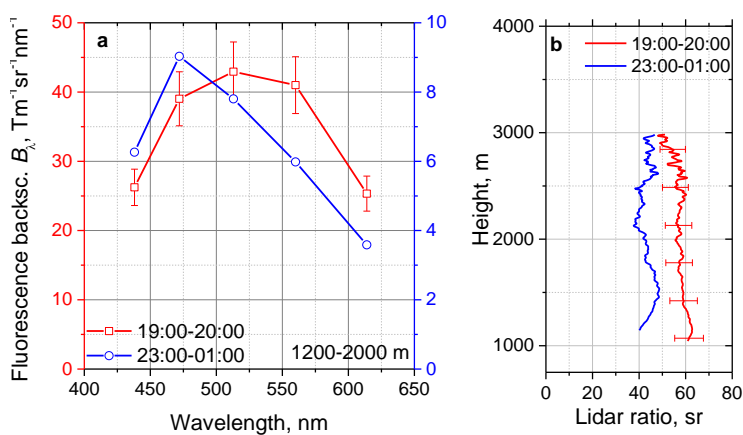


Fig.3. Spatio – temporal distribution of particle parameters on the night 27-28 August 2022. (left column) Aerosol backscattering coefficient  $\beta_{355}$ , fluorescence backscattering  $\beta_{F472}$  (in  $10^{-4} \text{ Mm}^{-1} \text{sr}^{-1}$ ), fluorescence capacity  $G_{472}$ . (right column) Ratios of fluorescence spectral backscattering coefficients  $B_{472}/B_{438}$ ,  $B_{472}/B_{513}$ ,  $B_{472}/B_{560}$ .



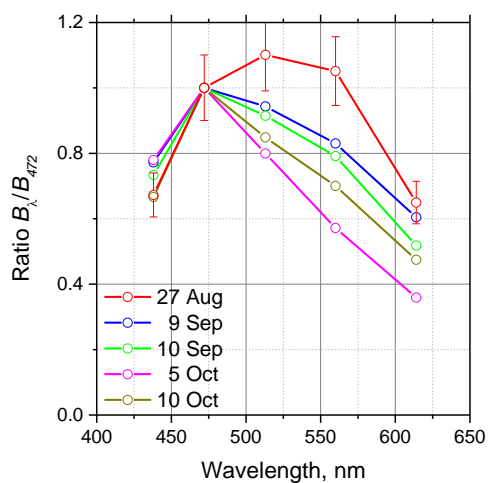
445  
 446 Fig.4. Observations on 27 August 2022 for period 19:00-20:00 UTC. (a) Fluorescence spectral  
 447 backscattering coefficients  $B_\lambda$  at 438, 472, 513, 560, 614 nm and the aerosol backscattering  
 448 coefficient  $\beta_{355}$ . (b) The ratios  $B_{472}/B_{438}$ ,  $B_{472}/B_{513}$ ,  $B_{472}/B_{560}$ ,  $B_{472}/B_{614}$  and the fluorescence  
 449 capacity  $G_{472}$ . Symbols show the relative humidity measured by a radiosonde at 00:00 UTC on  
 450 28 August.



451  
 452 Fig.5. (a) Spectrum of fluorescence backscattering  $B_\lambda$  on the night 27-28 August 2022 for 19:00-  
 453 20:00 and 23:00-01:00 UTC intervals. Results are averaged inside 1200-2000 m height range. (b)  
 454 Profiles of lidar ratios at 355 nm for the same temporal intervals.  
 455



456



457

458 Fig.6. Fluorescence spectra measured in September - October 2022, when forest fires were over.  
459 Fluorescence backscattering coefficients  $B_\lambda$  were averaged inside 500 – 1000 m height range and  
460 normalized on  $B_{472}$ . For comparison, the fluorescence spectrum in smoke plume on 27 August  
461 from Fig.5 is also presented.

462

463



464

465

466

467

468

469

470

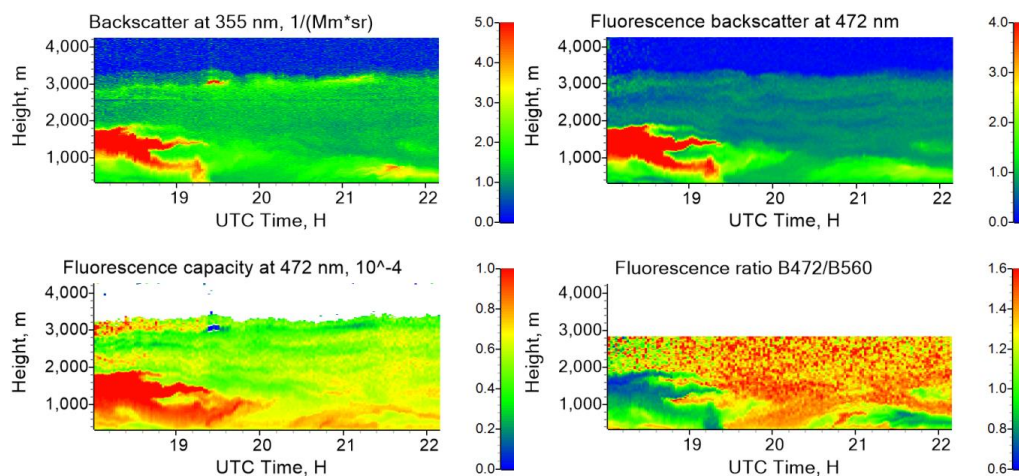
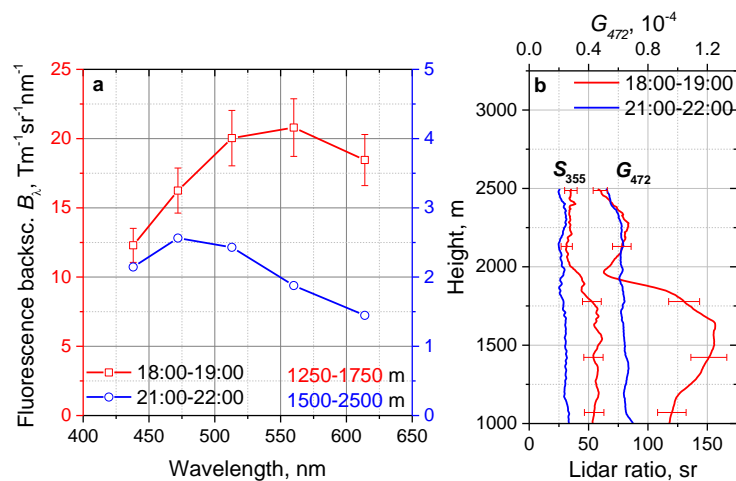


Fig.7. Observations on 17 August 2022. (left column) Aerosol backscattering coefficient  $\beta_{355}$  and fluorescence capacity  $G_{472}$ . (right column) Fluorescence backscattering coefficient  $\beta_{F472}$  (in  $10^{-4} \text{ Mm}^{-1} \text{ sr}^{-1}$ ) and the ratio of fluorescence spectral backscattering coefficients  $B_{472}/B_{560}$ .



471

472

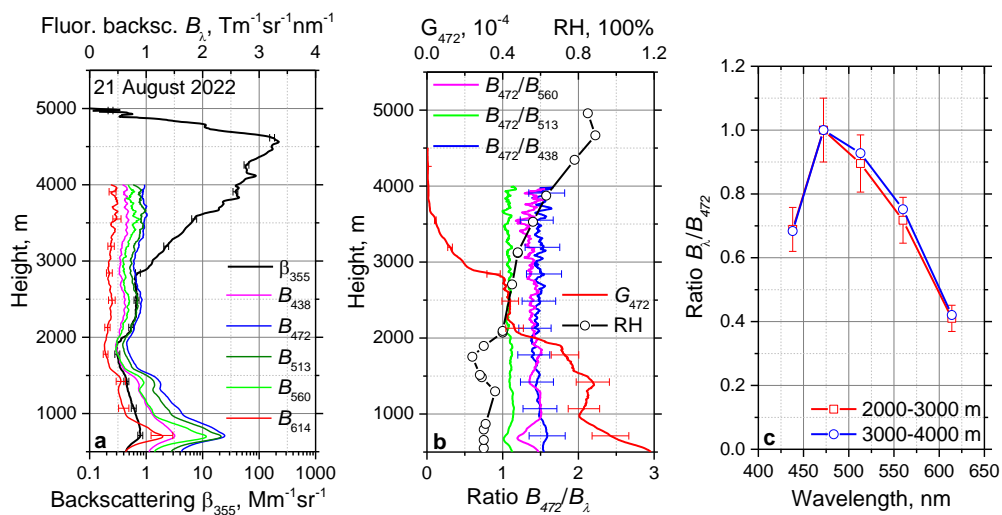
473

474

475

476

Fig.8. (a) Spectra of fluorescence backscattering  $B_{\lambda}$  on 17 August 2022 for 18:00-19:00 UTC and 21:00-22:00 UTC periods. Results are averaged within 1250-1750 m and 1500-2500 m height ranges respectively. (b) Profiles of lidar ratio  $S_{355}$  and fluorescence capacity  $G_{472}$  for the same temporal periods.



477

478 Fig.9. Vertical profiles of the particle parameters on 21 August 2022 for period 22:00-24:00  
 479 UTC. (a) The fluorescence spectral backscattering coefficients  $B_\lambda$  at 438, 472, 513, 560, 614 nm  
 480 and the aerosol backscattering coefficient  $\beta_{355}$ . (b) The ratios  $B_{472}/B_{438}$ ,  $B_{472}/B_{513}$ ,  $B_{472}/B_{560}$  and  
 481 the fluorescence capacity  $G_{472}$ . Symbols show the relative humidity measured by a radiosonde at  
 482 00:00 UTC on 22 August. (c) Spectrum of the fluorescence backscattering coefficient  $B_\lambda$  for  
 483 height intervals 2000-3000 m and 3000-4000 m. Values of  $B_\lambda$  are normalized on  $B_{472}$ .

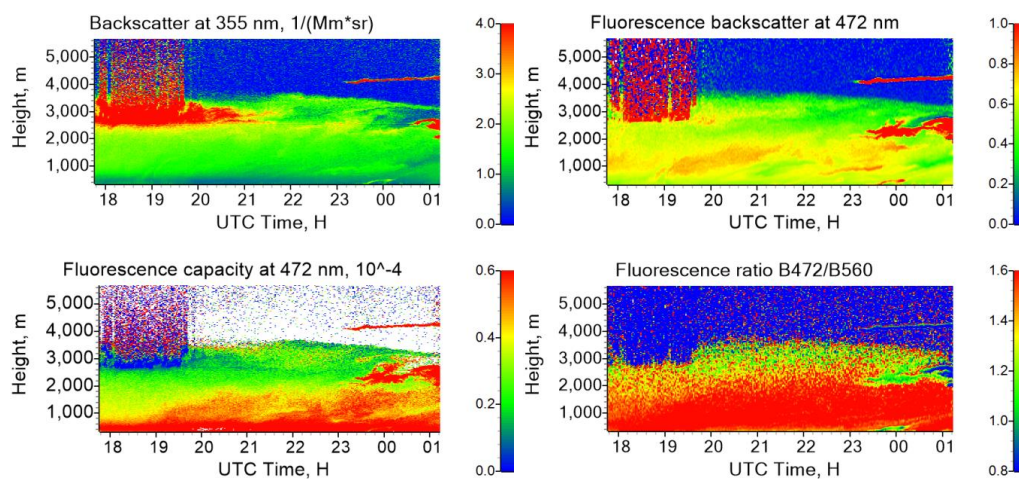
484

485





486



487

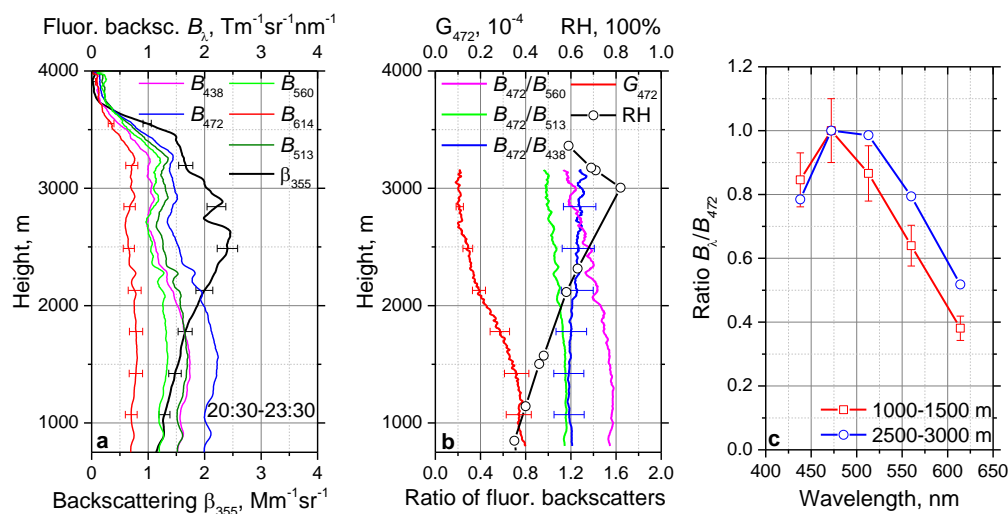
488 Fig.10. Spatio-temporal distributions of the particle parameters on the night 23-24 August 2022.  
489 (left column) The aerosol backscattering coefficient  $\beta_{355}$  together with the fluorescence capacity  
490  $G_{472}$ . (right column) The fluorescence backscattering coefficient  $\beta_{F472}$  (in  $10^{-4} \text{ Mm}^{-1} \text{ sr}^{-1}$ ) and the  
491 ratio  $B_{472}/B_{560}$ .

492

493



494



495

496

497 Fig.11. Vertical profiles of the particle parameters on 23 August 2022 for period 20:30-23:30  
 498 UTC. (a) The fluorescence spectral backscattering coefficients  $B_{\lambda}$  at 438, 472, 513, 560, 614 nm  
 499 and the aerosol backscattering coefficient  $\beta_{355}$ . (b) The ratios  $B_{472}/B_{438}$ ,  $B_{472}/B_{513}$ ,  $B_{472}/B_{560}$  and  
 500 the fluorescence capacity  $G_{472}$ . Symbols show the relative humidity measured by a radiosonde at  
 501 00:00 UTC on 24 August. (c) Spectrum of the fluorescence backscattering coefficient  $B_{\lambda}$  for  
 502 height intervals 1000-1500 m and 2500-3000 m. Values of  $B_{\lambda}$  are normalized on  $B_{472}$ .

503

504